CrossMark

ORIGINAL ARTICLE

SPH numerical investigation of characteristics of hydraulic jumps

Diana De Padova[1] · Michele Mossa[1] · Stefano Sibilla[2]

Abstract In the present work, oscillating characteristics and cyclic mechanisms in hydraulic jumps are investigated and reproduced using a weakly-compressible XSPH scheme which includes both an algebraic mixing-length model and a two-equation turbulence model to represent turbulent stresses. The numerical model is applied to analyze oscillations of different hydraulic jump types based on the laboratory experiments. The comparison between SPH and experimental results shows an influence of different turbulence models on the amplitude spectrum and peak amplitude of the time-dependent surface elevation upstream and downstream of the hydraulic jump. By analyzing a single cycle of the oscillating phenomena of a hydraulic jump it is possible to indicate their correlation with the vortex structures of the roller. Furthermore, analysis of the oscillating phenomena indicates a correlation among the surface profile elevations, velocity components and pressure fluctuations. This observation leads to conclude that oscillations phenomena are particularly important for analysis of the turbulence characteristics.

✉ Diana De Padova
  diana.depadova@poliba.it

  Michele Mossa
  michele.mossa@poliba.it

  Stefano Sibilla
  stefano.sibilla@unipv.it

[1] Department of Civil, Environmental, Land, Building Engineering and Chemistry (DICATECh), Polytechnic University of Bari, Bari, Italy

[2] Department of Civil Engineering and Architecture, University of Pavia, Pavia, Italy

1 Introduction

The hydraulic jump is the sudden flow transition which occurs when a supercritical flow is forced to become subcritical. This transition involves always a strong energy dissipation induced by the increase in turbulence intensity, which derives from the sudden flow deceleration, and results often in an intense turbulent roller [18, 72].

On the flow structure description, Resch and Leutheusser [74] reported turbulence quantities and pointed out dependence on the inlet flow conditions. Gualtieri and Chanson [35, 36] further analyzed the inlet sensitivity conditions. Additionally, Chanson and Brattberg [14], Murzyn et al. [63], Chanson and Gualtieri [16], and Zhang et al. [91] focused on the flow aeration properties.

Some researchers pointed out the existence of oscillating phenomena, and particularly of a cyclic variation of hydraulic jump types over long-lasting experiments, under specific flow conditions (e.g. [1, 38, 57, 58, 68, 70, 85, 86]).

The general definition of the oscillating characteristics of hydraulic jumps is referred to as a macroscopically visible feature of a hydraulic jump [58]. These oscillating characteristics can be: (a) change of one type of hydraulic jump to another; (b) horizontal movement of the hydraulic jump toe [45]; (c) variation of velocity components and pressure in the region close to the hydraulic jump roller; (d) formation, development and coalescence of the large-scale flow structures.

Some oscillating characteristics in the hydraulic jumps were evidenced by Nebbia's experiments [64–68] carried out in a channel with loose soil (sand and fine gravel) downstream of a horizontal apron. Nebbia noted that the mobility of the bottom was not the main cause of the flow oscillations.

Experiments by Ghafar et al. [1] on local scour due to hydraulic jump formed on the sand after a horizontal apron pointed out the existence of oscillating characteristics under different conditions. Analysis of those experiments showed that, for some runs, the hydraulic jump tended to repeat itself in a periodic form, from clockwise to anti-clockwise rotation of the vortex, and a period of the phenomenon was determined hence.

Further experiments by Mossa [58], carried out in a channel with non-erodible bottom presenting a moulded bed profile, took into account the previous studies to investigate the oscillating characteristics of hydraulic jumps. Mossa noted that the oscillations of the hydraulic jump were not linked to the presence of an erodible bed, but depended rather on the shape of this bed, either erodible or non-erodible, and on the hydrodynamic characteristics of the channel flow.

Moore and Morgan [56] suggested a classification of the hydraulic jumps at an abrupt drop which has been used by many authors. In this regard, it is possible to refer to Fig. 1 by Ohtsu and Yasuda [70]. Although this classification refers to the situation in which the cavity of the bed is created by an abrupt drop, the same terminology can be extended also to the cases where the non-erodible bed profile is more complex.

Modelling of hydraulic jump is usually rather demanding on numerical methods, because of its unsteady characteristics, including the propagation of short breaking waves which can lead to a non-accurate capturing of the free-surface [58]. Further details on the main characteristics of hydraulic jumps or hydraulic jump flow type are reported in Mossa et al. [59, 60], Mossa [61, 62] and Ben Meftah et al. [8–10].

Although successful simulations have been obtained by adopting purely Eulerian or mixed Eulerian–Lagrangian methods (see, for instance: [6, 13, 15, 17, 47, 51]), meshless Lagrangian techniques [21, 22, 30, 40, 64] appear in general to be more suitable to capture the complex and highly-unsteady free-surface patterns which characterize a hydraulic
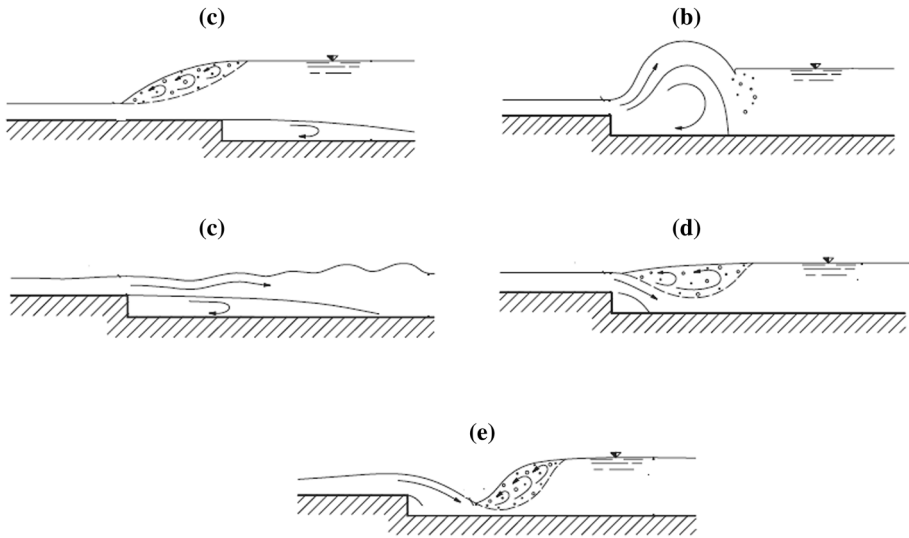
Fig. 1 Flow conditions (from Ohtsu and Yasuda [70]). From the top: **a** A-jump; **b** wave jump; **c** wave train; **d** B-jump (maximum plunging condition); **e** minimum B-jump (limited jump)

jump. SPH appears actually to be effective in solving several other free-surface problems with highly nonlinear deformation [84], such as wave breaking and impact [2, 19, 23, 42, 69, 71]; multi-phase flows for coastal and other hydraulic applications with air–water mixtures and sediment scouring [24, 31, 48, 49, 55, 78, 80]; long waves, e.g. floods, tsunamis and landslide submersions [5, 11]; flow around ships and ditching [12, 50, 90], oscillating jets inducing breaking waves [29]. The method is fully Lagrangian and obtains, through a discrete kernel approximation, the solution of the equations of motion for each of the fluid particles in which the flowing volume is discretized: the free surface requires, therefore, no special approach, such as in the case of the Volume-of-Fluid method or of Lagrangian surface tracking techniques. Furthermore, the method can easily treat rotational flows with vorticity and turbulence.

The SPH turbulence models used for engineering applications have been based on RANS (Reynolds-averaged Navier–Stokes) approaches with first-order closure (eddy viscosity models), using mixing length [83], k or k-ε models [81].

Both turbulence model were successfully applied to SPH analyses of rotational flows, such as wave overtopping [75], or spilling breakers [24].

The purpose of this paper is to use a weakly-compressible SPH scheme, together with either an algebraic mixing-length turbulence model or a two-equation turbulence model to study the oscillating characteristics and cyclic mechanisms in different hydraulic jump types, comparing the results with the laboratory experiments by Mossa [58] in order to obtain a deeper understanding of the physical features of the flow.

2 Modelling and software

2.1 SPH numerical method

SPH is a meshless, Lagrangian method for the numerical solution of convection–diffusion equations, where any continuous vector function characterizing the system flow is approximated by a discrete vector function defined in a suitable number of discrete moving points, each associated to an elementary material volume (or *particle*) i, which has position x_i and constant mass m_i [32, 46].

The reader is referred to general descriptions of SPH in textbooks and review articles, where further details on the different methods for SPH approximations can be found [33, 43, 44, 52, 53, 79, 82]. In the following, only the relevant, peculiar features of the SPH method used to obtain the present results will be described.

The core of the method relies on the choice of a *kernel* function $W_{ij} = W(x_i - x_j, \eta)$ which allows to interpolate any flow variable in the generic point x_i from the surrounding moving points x_j where the variable is computed. The kernel function needs to be continuous, non-zero only for $|x_i - x_j| < 2\eta$, where η is defined as the *smoothing length*, and tends to the Dirac delta function when η tends to zero. Here the C2 Wendland kernel function [88], which has been shown [26] to have better numerical convergence properties, was used to discretize the Reynolds-averaged Navier–Stokes equations for a weakly compressible fluid. In a Lagrangian frame, the full system of the equations of continuity, momentum, state and turbulent closure takes the following form:

$$\begin{cases} \dfrac{D\rho}{Dt} + \rho \nabla \cdot v = 0 \\ \dfrac{Dv}{Dt} = -\dfrac{1}{\rho}\nabla p + \dfrac{1}{\rho}\nabla \cdot \mathcal{T} + \mathbf{g} \\ p - p_0 = c^2(\varrho - \rho_0) \\ \mathcal{T} = \mu_T \mathcal{S} \end{cases} \tag{1}$$

where $v = (u, v)$ is the velocity vector, p is pressure, g is the gravity acceleration vector, $\mathcal{T}$ is the turbulent shear stress tensor, c is the speed of sound in the weakly compressible fluid, μ_T is the dynamic eddy viscosity, $\mathcal{S}$ is rate-of-strain tensor and the subscript 0 denotes a reference state for pressure computation. All the variables in Eqs. (1) are assumed to be Reynolds-averaged.

The Weakly Compressible SPH (WCSPH) here followed consists in adopting the weakly compressible formulation (1) with a reduced value of the speed of sound, which takes therefore the role of a numerical parameter. Monaghan [52] demonstrated that the error associated with the adoption of a compressible formulation for the incompressible free-surface water flow is bounded to 1%, provided the local numerical Mach number $M_i = |v_i|/c_i$ be everywhere lower than 0.1. After applying the SPH space-discretization, Eqs. (1) become:

$$\begin{cases} \left\langle \dfrac{\mathrm{D}\rho_i}{\mathrm{D}t} \right\rangle = \sum_j m_j (\boldsymbol{v}_i - \boldsymbol{v}_j) \cdot \nabla \widehat{W_{ij}} \\[2mm] \left\langle \dfrac{\mathrm{D}\boldsymbol{v}_i}{\mathrm{D}t} \right\rangle = -\sum_j m_j \left(\dfrac{p_i}{\rho_i^2} + \dfrac{p_j}{\rho_j^2} \right) \nabla W_{ij} + \sum_j m_j (\mathcal{T}_i - \mathcal{T}_j) \cdot \nabla \widehat{W_{ij}} + \mathbf{g} \\[2mm] p_i - p_0 = c_i^2 (\varrho_i - \rho_0) \\[2mm] \mathcal{T}_i = \mu_{Ti} \mathcal{S}_i \end{cases} \qquad (2)$$

where the angle brackets indicate the SPH approximation. The notation $\widehat{W_{ij}}$ in (2) is used to indicate in brief a renormalizion procedure for the SPH kernel approximation which enforces consistency on the first derivatives to the desired order [77]. Here the procedure is used to enforce 1st order consistency (leading to a 2nd order accurate discretization scheme in space) on the SPH evaluation of velocity divergence term in the continuity equation, of the local rate-of-strain tensor and of the divergence of the stress tensor in the momentum equation. The pressure gradient term is instead written in a form which guarantees momentum conservation [53, 82].

The semi-discretized system (2) is integrated in time by a 2nd order two-stage XSPH explicit algorithm [52], where momentum equation is solved in the first stage to yield the velocity field $\boldsymbol{v}^{n+1}$ at the new time step, while a smoothed velocity:

$$\hat{\boldsymbol{v}}_i = (1 - \varphi_v) \boldsymbol{v}_i^{n+1} + \varphi_v \sum_j \frac{m_j}{\rho_j} \boldsymbol{v}_i^{n+1} \widehat{W_{ij}} \qquad (3)$$

where φ_v is a velocity smoothing coefficient. The smoothed velocity value is then used to update the particle position and to solve the continuity equation.

In order to reduce the numerical noise in pressure evaluation which affects WCSPH owing to high frequency acoustic signals [3]. A similar smoothing procedure was applied to the difference between the local and the hydrostatic pressure values [22, 76], with an approach alternative to other methods proposed to reduce pressure oscillations in WCSPH, such as δ-SPH [4], where a numerical diffusive term for density is added to the continuity equation.

Ghost particles are used to impose wall boundary conditions [73], while the super-critical inflow condition is enforced through the introduction of a $2h$-wide layer of fluid particles with constant velocity and head along the water depth.

The eddy viscosity μ_T in (2) must be evaluated through a proper turbulence model. Bayon et al. [6] adopted in their Finite Volume hydraulic jump simulations the k-ε RNG model [89]: although in principle this model contains an additional term in the dissipation equation which should provide a higher sensitivity to rapid strain and streamline curvature, literature results are not unanimous in determining whether its use should always be preferred in comparison to other turbulence models, when dealing with vortex and/or swirling flows (see, for instance [28, 37]). Previous SPH simulations of hydraulic jumps [22, 25] suggest instead to test the application of either a mixing-length or a standard k-ε model. In the first one, the mixing-length for each particle is proportional to its distance from the wall, multiplied by a damping function which avoids its non-physical growth close to the free-surface. The two-equation model is a SPH version of the standard k-ε turbulence model by Launder and Spalding [41]. Both models were described in De Padova et al. [22] to which the reader is referred to for further details.

Finally, it must be noted that aeration plays in general an important role in the dynamics of the hydraulic jump roller and a multi-phase SPH analysis [39, 54, 87] could be advisable to model this phenomenon. However, air entrainment in hydraulic jumps gives rise to a

dispersed bubbly flow, and although the SPH modeling of bubble flows is at present feasible in the case of bubble rising or merging [34], its application to a general, dispersed bubbly flow can be very demanding from the computational point of view and its reliability is still questionable. Moreover, the validation of an accurate model for air entrainment in a hydraulic jump is outside the scope of the present paper, which is aimed at the analysis of flow oscillations.

On the other hand, the fact that the onset of flow oscillations is primarily related to the submergence ratio and to the effect of the separation of the flow along the channel bed, where air entrainment is less relevant, allows one to obtain a consistent simulation of the flow also by using a single-phase description. This approach proved to be effective in other cases of hydraulic jump simulations [22, 25], where air entrainment also plays an important role but consistent results can be obtained also through a single-phase analysis.

2.2 PVSPH software details

The numerical procedure outlined in Sect. 2.1 was implemented in the Fortran 95 PVSPH code, developed at the Fluid Mechanics Laboratory of the Department of Civil Engineering and Architecture of the University of Pavia (Italy).

The data structure of the code is influenced by the peculiarities of the method. Differently from mesh-based methods, a pre-defined mesh topology cannot be defined: therefore, each summation extended to the *neighbors* (i.e. the particles j surrounding a given space location x_i) refers, at every time step, to a different set of particles, which must be recomputed after every particle displacement.

On one hand, this feature is the greatest strength of the method, because it allows one to obtain a perfect adaptivity to moving boundaries and free surfaces; on the other hand, it is computationally demanding and poorly efficient, mainly because:

- it requires the check of the inequality $|x_i - x_j| < 2\eta$ on the relative distance for every particle pair, with a number of operations proportional to N^2, where N is the total particle number;
- particle quantities are contained in arrays which are indexed by particle numbers, which are in general non-contiguous within a single particle domain of influence: data reloading by the cache memory occurs therefore continuously whenever a summation on particles is performed, increasing computational times.

These drawbacks were faced in PVSPH by a twofold strategy:

- the *neighbor* search is performed through a *cell-linked list* algorithm: the computational domain is first divided in a regular Cartesian grid with $2h$ cell spacing, particle addresses are then stored according to the cell they belong to, and the distance inequality is therefore verified only on the particles belonging to the subset of the closest cells [27];
- quantities such as $m_j/\rho_j W_{ij}$ and $m_j/\rho_j \vec{\nabla} W_{ij}$ are computed during the neighbor list building and stored in arrays indexed by local particle addresses within the neighborhood: in this way, although increasing the overall memory requirements, the access to contiguous data in the CPU memory results in a consistent reduction of computational times.

Parallelization of the PVSPH code on shared memory systems was obtained by use of the OpenMP libraries, with a parallelization at loop level for every summation cycle

needed to compute the right-hand side terms in Eq. (2), as well as in the smoothing procedures such as (2). The parallel PVSPH code was successfully tested both on multi-processor multi-core architectures, both on Microsoft Windows and Linux systems.

3 Experimental set up and validation data

The results obtained from the numerical model outlined in the previous section were validated against extensive experimental data, and then used to obtain further insight in the physics of the peculiar hydraulic jump case here analysed.

Experimental investigations were carried out in the hydraulic laboratory of the Mediterranean Agronomic Institute (hereafter referred to as IAM) in Valenzano (Bari, Italy) in a 7.72-m long 0.3-m wide rectangular channel with sidewall height of 0.40 m (Fig. 2). The walls and bottoms of both channels were made of Plexiglas.

Discharges were measured by a triangular sharp-crested weir. Measurements of upstream and downstream water depths were carried out with electric hydrometers type point gauges supplied with electronic integrators which yielded directly the estimate of the time-averaged flow depth. The hydrometers, supplied with verniers, have a measurement accuracy of ± 0.1 mm. Water discharge and tailwater depth were regulated by two gates placed, respectively, at the upstream and downstream ends of the channel. Figure 3 shows the shape of the wooden bed which has been used to reproduce a fixed scoured bed. The profile coincides with one of those measured by Abdel Ghafar et al. [1] in the central longitudinal section of the channel, when equilibrium scour profiles were reached.

Table 1 lists the main experimental parameters of the investigated hydraulic jumps: Q is the discharge; y_1 is the water depth in Sect. 2, located at the downstream end of the horizontal apron, i.e. where the cavity begins; y_t is the water depth downstream of the hydraulic jump, where a second horizontal apron is located; $F_1 = V_1/(gy_1)^{0.5}$ is the Froude number in Sect. 2 and $Re = V_1y_1/\nu$ is the Reynolds number, where V_1 indicates the mean

Fig. 2 Picture of the channel at the Hydraulic laboratory of the Mediterranean Agronomic Institute (IAM) of Valenzano. During the experiments on scour holes by Ben Meftah and Mossa [7]
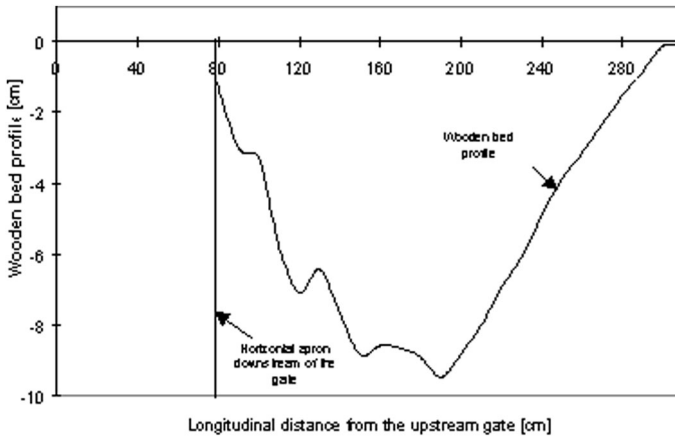
Fig. 3 Shape of the wooden bed used for configurations carried out in the channel

Table 1 Experimental parameters of the analysed hydraulic jumps

Test	Run no. [58]	Q (l/s)	y_1 (cm)	y_t (cm)	y_1/y_t	F_1	Re	Jump type
T1	8V1	12.7	1.94	10.43	5.38	4.99	42,193	B and wave
T2	20V1	9.60	2.50	7.70	3.08	2.58	31,894	B and wave
T3	21V1	9.60	1.90	7.90	4.16	3.89	31,894	B and wave
T4	22V1	9.33	2.40	7.60	3.17	2.66	30,997	B and wave
T5	12V1	12.02	1.84	13.39	7.28	5.11	39,933	A
T6	1V1	21.87	4.20	10.19	2.43	2.70	72,658	B

Run number refers to the experiments listed in the reference paper by Mossa [58]

velocity of the supercritical flow in Sect. 2, v the water kinematic viscosity and g the gravity acceleration. During all experiments, water temperature was measured by a thermometer with an accuracy of 10^{-1} C.

In some tests a video camera filmed the roller area and the area close to is so that the hydraulic jumps could be carefully analyzed. A special resistance probe fitted with two metallic tips of different lengths connected with an electronic conditioner was also used. Its output, consisting in a positive signal when the tips were both dipped in the water, and in a negative one when the shorter tip was in air, proved to be useful to identify the configurations with cyclic oscillations of the hydraulic jump types, by measuring the duration of the time intervals when wave type (open probe circuit) and, respectively, type A or B (close probe circuit) are present. The probe was placed just upstream of the hydraulic jump when it was of the wave type, setting it in order to dip only the longer tip in water, obtaining an open circuit and a negative signal from the electronic conditioner. When the hydraulic jump type shifted to A or B, i.e. the typical hydraulic jump configuration with roller generation and consequent rise of tailwater depth, the circuit closed and a positive signal was obtained.

A resistance probe for the measurement of the surface profile was placed downstream of the roller. The signals of both probes were simultaneously sampled by a process computer

supplied with an A/D and D/A electronic board by National Instruments, model AT-MIO 16 H. For further details see Mossa [58].

4 Numerical tests and results

### 4.1 Domain dimension and numerical parameters

As stated above, the simulation of hydraulic jumps were conducted to assess SPH model accuracy using experimental data by Mossa [58]. The 2D simulations reported in Table 1 were performed in a physical domain consisting in a rectangle 3.3 m long and 0.4 m high, i.e. shorter than the real channel in the test facility. The shorter domain was chosen in order to reduce the computational cost without influencing the quality of the numerical solution.

According to previous sensitivity analyses performed on hydraulic jump and breaking wave flows [22, 24], the SPH simulations of these experimental hydraulic jump tests were performed by adopting a velocity smoothing coefficient in the XSPH scheme $\varphi_v = 0.01$. It can be seen that the simulations with a higher ($\varphi_v = 0.02$) and lower ($\varphi_v = 0.005$) velocity smoothing coefficient are not able to predict the oscillating characteristics and cyclic mechanisms in hydraulic jumps (Figs. 4a, 5b). A value $\varphi_v = 0.01$ guarantees the stability of the SPH solutions without affecting the quality of the numerical results and therefore it was chosen.

The ratio of the smoothing length to the initial particle spacing Σ influences the efficiency of the SPH kernel function [26] and that its value should be at least $\eta/\Sigma \geq 1.2$ [20].

Here, a constant value of $\eta/\Sigma = 1.5$ was maintained for all the simulations and a convergence analysis was carried out for test. Simulations were performed by choosing a coarser and a finer initial particle spacing Σ; In particular, the 2D flow was simulated by discretizing the computational domain with Σ ranging from 0.022 to 0.005 m.

The related number of SPH particles N_p in the computational domain ranged from about 1000 to 19,000, respectively. It can be seen that the simulation at the lowest resolution is not able to predict the oscillating characteristics and cyclic mechanisms in hydraulic jumps. Results of the sensitivity analysis highlight that, if an initial particle spacing $\Sigma \leq 0.008$ m is adopted, SPH simulations show results in accordance with the experiments. Therefore, all the SPH simulations have been then performed with an initial particle spacing $\Sigma = 0.008$ m and $\eta/\Sigma = 1.5$.
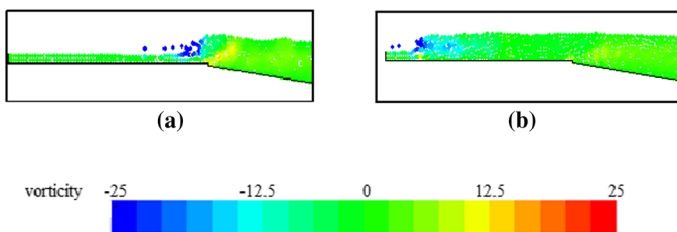
Fig. 4 Instantaneous SPH vorticity field in the SPH simulation of Test T3a with a velocity smoothing coefficient φ_v equal to 0.005: **a** t = 4 s; **b** t = 12 s
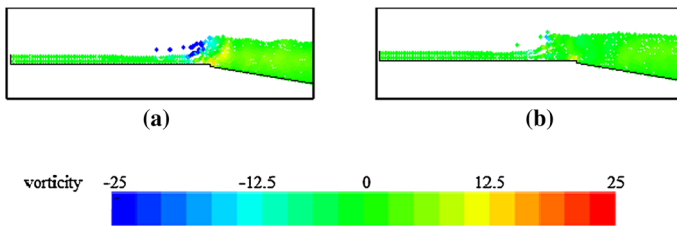
Fig. 5 Instantaneous SPH vorticity field in the SPH simulation of Test T3a with a velocity smoothing coefficient φ_v equal to 0.02: **a** t = 4 s; **b** t = 12 s

4.2 Choice of the turbulence model

The sensitivity to the turbulence model was also investigated and, similarly to the analysis shown by De Padova et al. [22], test T3 was repeated by adopting both a mixing length turbulence model with $l_{max} = 0.5\ h_2$ and the two-equation model (10).

Table 2 summarizes the principal characteristics of the simulations in the sensitivity analysis.

Both the mixing length model and the k-ε model yield similar results and are able to predict the oscillating characteristics and cyclic mechanism with oscillations between the B and wave jump which characterize this hydraulic jump. The instantaneous vorticity fields (Figs. 6a, 7d) clearly indicate that the transition phase between the two hydraulic jump types is well reproduced by both turbulence models (T3a and T3b). Vortices are characterized by a clockwise or anti-clockwise rotation, depending on which type of hydraulic jump is present. In particular, vortices are characterized by a clockwise rotation when the wave jump occurs (Figs. 6a–c, 7a–c) and by an anti-clockwise one for the B jump (Figs. 6b–d, 7b–d), respectively.

Figure 8a, b show the amplitude spectra of the time series of the surface elevations for tests T3a and T3b, upstream and downstream of the hydraulic jump. From the analysis of the previous figures it is possible to observe the existence of a peak in each spectrum, as it was shown in the experiments by Mossa [58]: the oscillating characteristic of these hydraulic jumps can be therefore considered to be quasi-periodic. Furthermore, as the spectra in Fig. 6b show a peak at a frequency similar to the ones in Fig. 8a, it is possible to conclude that the fluctuations of the surface profile downstream of the hydraulic jump depend on the alternation between wave and B types.

Although both turbulence models yield similar results, the detailed comparison of the amplitude spectra of the time series of the surface elevations upstream and downstream of the hydraulic jump for tests T3a and T3b, shows that the results obtained with the mixing-length model are closer to the experimental data than the k-ε ones (Fig. 8a, b). In particular,

Table 2 Numerical parameters of the SPH simulations in the sensitivity analysis

Test	Turbulence model	η/Σ	N_P
T3a	Mixing-length model	1.5	6000
T3b	k-ε turbulence model	1.5	6000
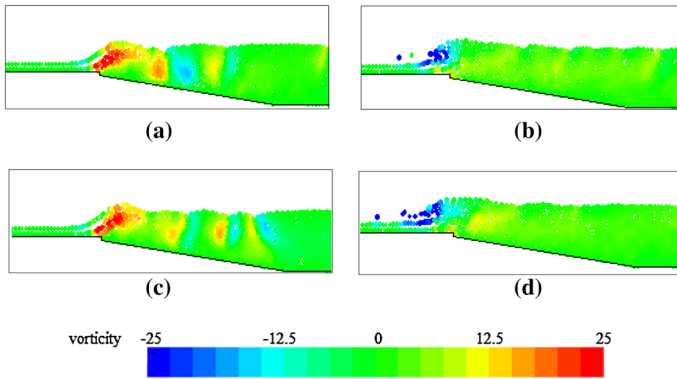
Fig. 6 Instantaneous SPH vorticity field in the SPH simulation of Test T3a: **a** t = 30 s; **b** t = 34 s; **c** t = 38 s; **d** t = 42 s
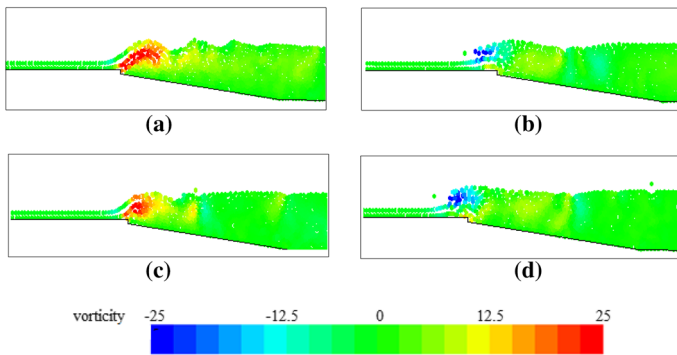
Fig. 7 Instantaneous SPH vorticity field in the SPH simulation of Test T3b: **a** t = 10 s; **b** t = 12 s; **c** t = 14 s; **d** t = 16 s

the two- equation turbulence model overestimates the peak amplitude of the fluctuations of the surface elevation upstream, while predicting a lower main frequency.

Actually, each spectrum shows a peak frequency, which is slightly higher than 0.1 Hz for test T3a, as shown by Mossa [58], and lower than 0.1 Hz for test T3b. In particular, Fig. 8b shows a better agreement between numerical results of Test T3a and measurements at two different sampling frequencies, in term of the amplitude spectrum of the time-dependent surface elevation downstream of the hydraulic jump.

Therefore, all the remaining SPH simulations (tests T1, T2, T4, T5 and T6) were performed only with the mixing-length turbulence model.

4.3 Analysis of stable versus oscillating flow behavior

The previous analysis highlights also the main characteristics of this phenomenon, which under specific flow conditions can lead to cyclic oscillations between hydraulic jump types, resulting in the cyclic formation and evolution of hydraulic jump vortices. The results of some other flow conditions here tested (T1, T2, T4) confirm the conclusions previously discussed for test T3, while other conditions (T5 and T6) lead to stable states.
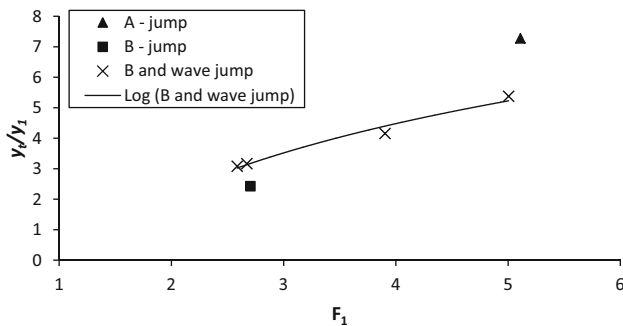
Fig. 8 Amplitude spectrum of the time series surface profile **a** upstream and **b** downstream of the hydraulic jump for the SPH simulations of test T3 and two different turbulence models: mixing-length (T3a) and k-ε (T3b)
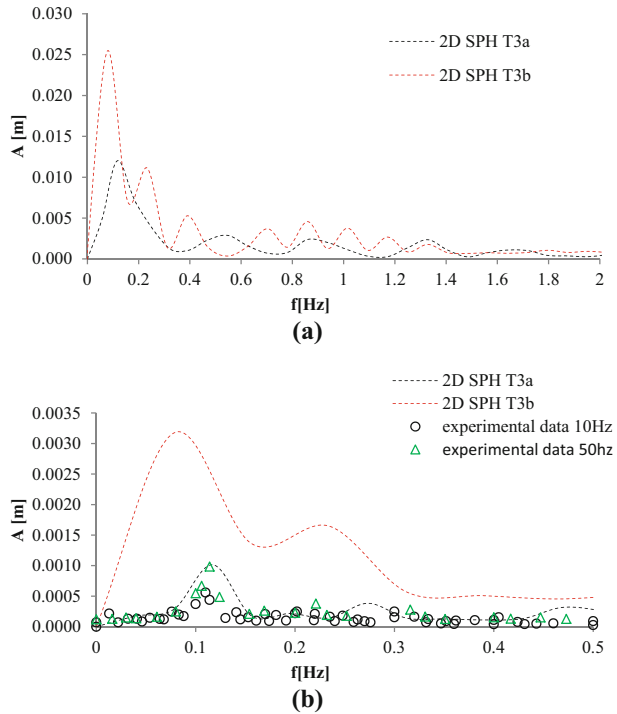
The diagram in Fig. 9 shows the different behaviors of the simulated flows as a function of the Froude number F_1 and of the ratio y_1/y_t.

It can be seen that the configurations in which cyclic oscillations of the hydraulic jump type appear (represented by cross symbols) identify a boundary between two adjacent regions where stable hydraulic jump flows occur. Actually, SPH simulations of the flows with lower Froude number (T2, T4 and T6) showed that a slight variation of the downstream gate opening proved to be sufficient, under the same upstream conditions, to shift from a stable to an oscillating flow configuration.

Figures 10, 11 and 12 show amplitude spectra of the surface elevation upstream and downstream of the hydraulic jump for tests T1, T2, and T4. From the analysis of these
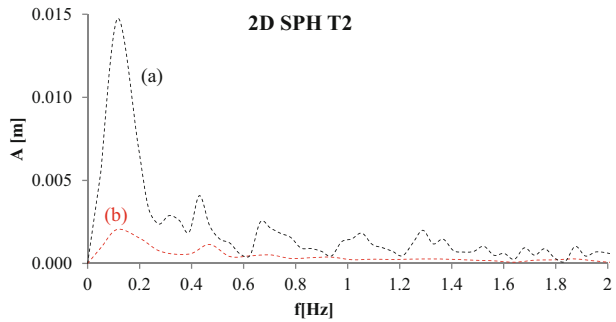
Fig. 9 Regime chart for simulated hydraulic jumps

Fig. 10 Amplitude spectrum of the time series surface profile **a** upstream and **b** downstream of the hydraulic jump for the SPH simulations of test T1
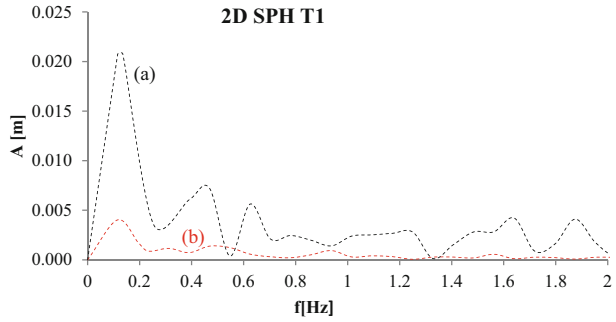
Fig. 11 Amplitude spectrum of the time series surface profile **a** upstream and **b** downstream of the hydraulic jump for the SPH simulations of test T2

Fig. 12 Amplitude spectrum of the time series surface profile **a** upstream and **b** downstream of the hydraulic jump for the SPH simulations of test T4
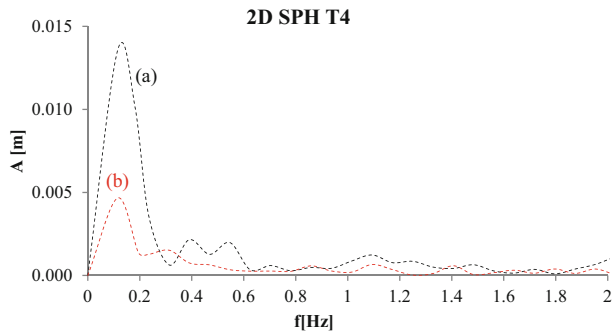
spectra it is possible to observe in each of them the existence of a peak at a frequency around 0.1 Hz, as shown by Mossa [58]. Consequently, the oscillating characteristic of these hydraulic jumps between wave and B type can be considered as quasi-periodic. Furthermore, as the frequency of the peak in the upstream spectra is almost equal to the downstream one, it is reasonable to assume that also in these cases the surface fluctuations downstream of the hydraulic jump depend essentially on the alternation of hydraulic jump types and that the small waves downstream of the hydraulic jump are produced by the quasi-periodic shift between different hydraulic jump types.

Figures 13a–d and 14a–d show a part of the time series and the amplitude spectra of the pressure measured at the bottom under the hydraulic jump T3 of Table 2. In particular, the pressure was measured at a distance of 7, 14, 20 and 100 from the time-averaged position of the hydraulic jump toe.

Fig. 13 Time series of the pressure under hydraulic jump (configuration: T3) measured at a distance of: **a** 7 cm; **b** 14 c; **c** 20 cm and **d** 100 cm from the time-averaged position of the hydraulic jump toe
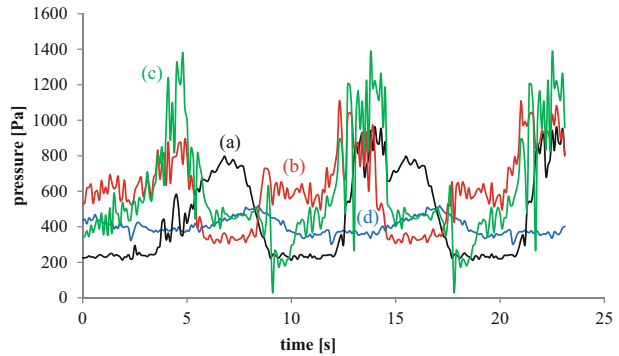
Fig. 14 Amplitude spectrum of pressure fluctuations under hydraulic jump (configuration: T3) measured at a distance of: **a** 7 cm; **b** 14 c; **c** 20 cm and **d** 100 cm from the time-averaged position of the hydraulic jump toe
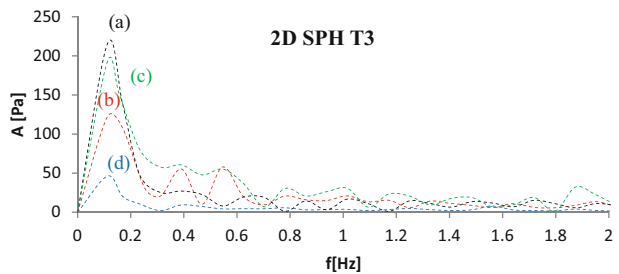

From the analysis of the pressure amplitude spectra it is clear that even the pressure fluctuations are quasi-periodic and strongly influenced by the oscillations between the B and wave types, as they show a peak amplitude at the same frequency of the elevation spectra. Moreover, it can be seen from the pressure time history that, in the point closest to the hydraulic jump toe, the bottom pressure assumes alternatively low and high pressures which can be mostly related to low and high water levels.

Downstream, the cycle between low and high pressures is less regular, possibly because of the simultaneous effect of level fluctuations due to waves and of turbulent pressure fluctuations downstream of the roller.

Figure 15a–d show the velocity magnitude field and the velocity vector field at selected instants of the SPH simulation of Test T3a with indication of the sections where the horizontal u and vertical v velocity components were computed. The alternation between the wave-jump (Fig. 15a, c) and the B-jump patterns (Fig. 15b, d) is evident and results, downstream of the hydraulic jump, in high-velocity regions flowing alternatively close to the surface or close to the bottom.

Figures 16a–d, 17a–d, 18a–d and 19a–d show a part of the time history and the amplitude spectrum of the horizontal u and vertical v velocity components computed at a point 0.01 m above the channel bottom under the hydraulic jump T3 of Table 2, at a distance of 7 cm, 14, 20 and 100 cm from the time-averaged position of the hydraulic jump toe. The analysis of the fluctuations of the velocity components for the configurations T3, characterized by the oscillations between B and wave types, shows also in this case the presence of a clearly dominant peak at the same frequency of 0.1 Hz.

Therefore, the analysis of the oscillating phenomena indicates a correlation among the surface profile elevations, velocity components and pressure fluctuations.
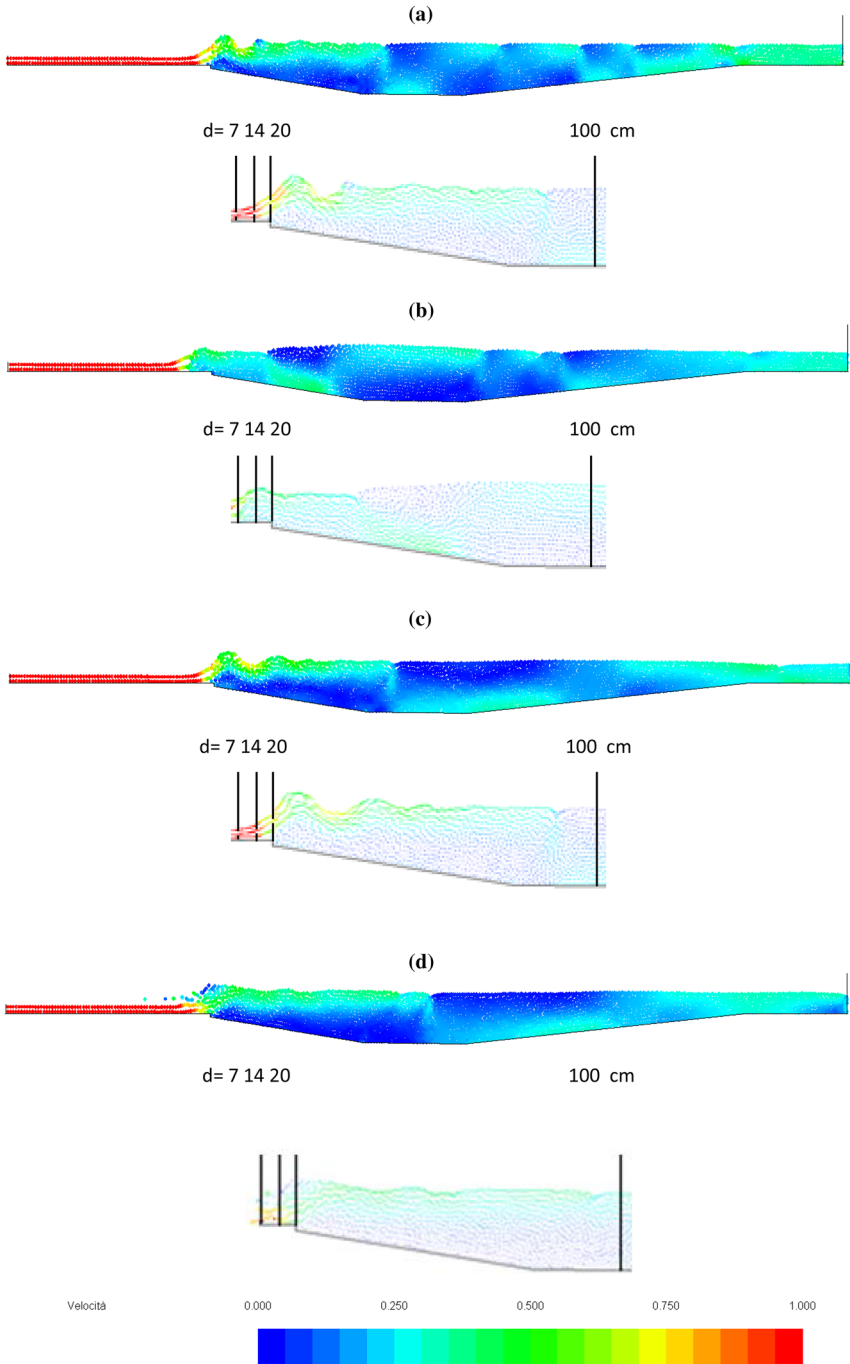
Fig. 15 Instantaneous SPH velocity field in the SPH simulation of Test T3a with indication of the sections where the velocity was computed: **a** t = 2 s; **b** t = 7 s; **c** t = 11 s; **d** t = 15 s
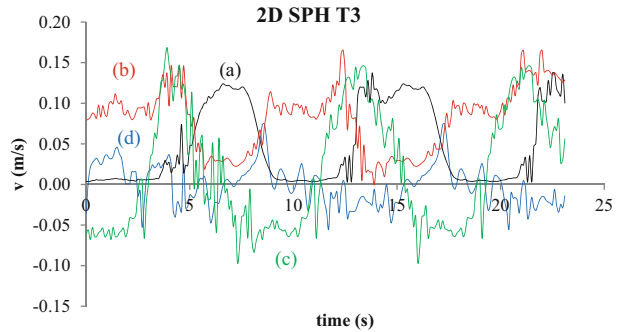
Fig. 16 Time series of the horizontal velocity component under hydraulic jump (configuration: T3) measured at a distance of: **a** 7 cm; **b** 14 c; **c** 20 cm and **d** 100 cm from the time-averaged position of the hydraulic jump toe
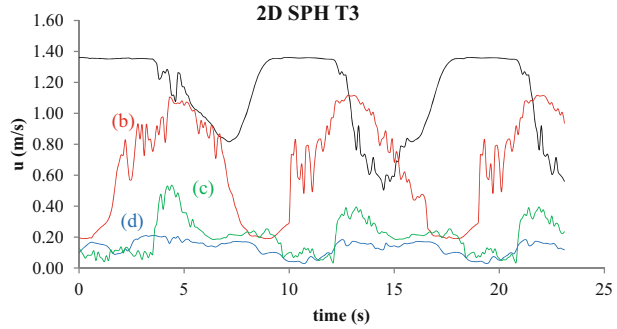
Fig. 17 Amplitude spectrum of the horizontal velocity component under hydraulic jump (configuration: T3) measured at a distance of: **a** 7 cm; **b** 14 c; **c** 20 cm and **d** 100 cm from the time-averaged position of the hydraulic jump toe
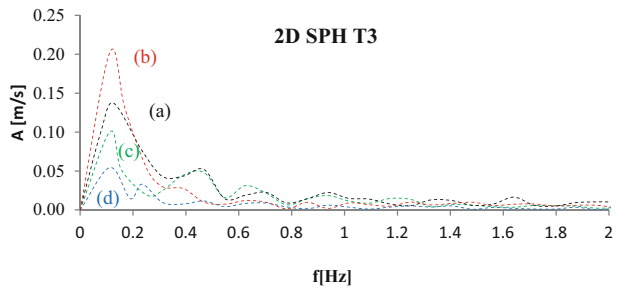
Fig. 18 Time series of the vertical velocity component under hydraulic jump (configuration: T3) measured at a distance of: **a** 7 cm; **b** 14 c; **c** 20 cm and **d** 100 cm from the time-averaged position of the hydraulic jump toe

Fig. 19 Amplitude spectrum of vertical velocity component under hydraulic jump (configuration: T3) measured at a distance of: **a** 7 cm; **b** 14 c; **c** 20 cm and **d** 100 cm from the time-averaged position of the hydraulic jump toe
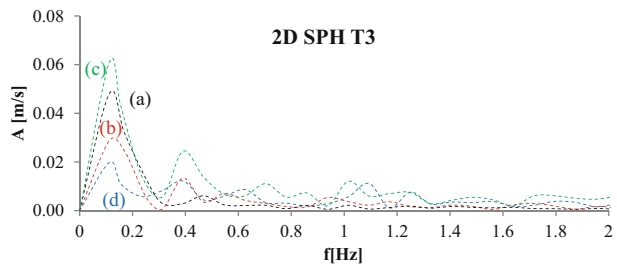
Actually, the analysis of the time histories of the velocity components in the first 24 s, as reported in Figs. 16 and 18, evidences three periods (roughly from 0 to 3 s, from 9 to 12 s and from 17 to 21 s) where the flow under the roller is very regular and directed horizontally, then shifts towards the surface and further downstream plunges again towards the bed: this behaviour is consistent with a wave-jump configuration. Approximately, these periods are the same when pressures/water levels are low near the average toe position, indicating that in general the hydraulic jump toe moves slightly forward when the wave-jump configuration occurs.

Conversely, in the two remaining periods (roughly, from 4 to 8 s and from 13 to 16 s) the flow appears to be less regular and is directed upwards just downstream of the jump toe and below the surface roller, consistently with a B-jump pattern and with a jump toe moving slightly upstream of its average position.

For a quantitative evaluation of the strength and the direction of a linear relationship between these variables, we computed the correlation coefficient r:

$$r = \frac{\sum_{i=1}^{n} \left[(x_{1_i} - \overline{x_1})(x_{2_i} - \overline{x_2}) \right]}{\sqrt{\sum_{i=1}^{n} (x_{1_i} - \overline{x_1})^2 \sum_{i=1}^{n} (x_{2_i} - \overline{x_2})^2}} \tag{4}$$

in which x_1 and x_2 are the two variables values, respectively, while the bar denotes an average of the two variables values.

The computed values of r for $(p–u)$, $(p–v)$ and $(u–v)$ pairs of data at a distance of 7 cm from the time–averaged position of the hydraulic jump toe, are equal to -0.97, 0.96 and -0.94, respectively, confirming that, near the time–averaged position of the hydraulic jump toe, p and v have a strong correlation while u is negatively correlated to both v and p. This again shows that the pattern shifts here between a low-level condition upstream of the wave-jump, where the flow is almost horizontal (Fig. 15a–c), and a steep rise of the flow due the wave-jump onset (Fig. 15b–d).

Figure 20a–c show a plot of the correlation coefficient r for $(p–u)$, $(p–v)$ and $(u–v)$ pairs of data measured at a distance (d) of 14, 20 cm and 100 cm from the time-averaged position of the hydraulic jump toe. In the points downstream of the hydraulic jump, the values of the correlation coefficients indicate a tendency to higher near-wall velocities when the water depth is higher, i.e. during the B-jump phase.

Farther downstream the two velocity components are substantially uncorrelated, indicating that the characteristic flow pattern of alternate near-wall and subsurface streams does not imply any preferential direction of the vertical motions.

Fig. 20 Plot of r versus (d) for $(p–u)$, $(p–v)$ and $(u–v)$ pairs of data (configuration: T3)
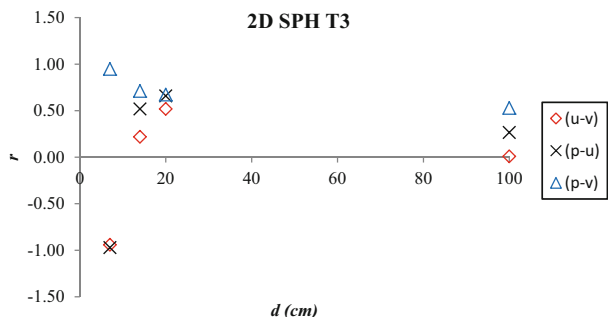
5 Conclusions

A 2D SPH scheme was applied to model numerically the cyclic mechanisms in hydraulic jumps realized in the hydraulic laboratory of the Mediterranean Agronomic Institute of Valenzano (Bari). The agreement between the numerical results and laboratory measurements is satisfactory and confirms the validity of the numerical tools to reproduce the peculiar features of the flow. The oscillating characteristics and cyclic mechanisms in hydraulic jump are investigated and reproduced using a weakly-compressible XSPH scheme which includes both an algebraic mixing-length model and a two-equation turbulence model to represent turbulent stresses.

Both the mixing length model and the k-ε model are able to predict the oscillating characteristics and cyclic mechanisms in hydraulic jumps.

By analyzing a single cycle of the oscillating phenomena of a hydraulic jump (periodic formation of different hydraulic jump types) it is possible to indicate their correlation with the vortex structures of the roller. Vortices were characterized by a clockwise or anti-clockwise rotation depending on which type of hydraulic jump was present. In particular, vortices were characterized by a clockwise rotation in the presence of the wave jump and an anti-clockwise one for the B jump respectively.

Although both turbulence models yielded similar results, the detailed comparison of the amplitude spectra of the time series of the surface elevations upstream and downstream of the hydraulic jump for the configuration T3, shows that the mixing-length results are closer to the experimental data than the k-ε ones. The comparison between SPH and experimental results shows an influence of different turbulence models, such as mixing length or Standard k-ε, on the amplitude spectrum and peak amplitude of the time-dependent surface elevation upstream and downstream of the hydraulic jump. As observed experimentally by Mossa [58], these numerical results show the existence of a peak at a similar frequency in both amplitude spectra of the surface elevations upstream and downstream of the hydraulic jump. It is possible to conclude that the fluctuations of the surface profile downstream of the hydraulic jump depended on alternations of jump types, and that the periodic formation of different hydraulic jump types produces small waves downstream of the hydraulic jump.

For all the configurations characterized by the oscillations between the B and wave types, the SPH model reproduces correctly the presence of a clearly dominant peak in the amplitude spectra of the time series of the surface elevations upstream and downstream of the hydraulic jump, in the amplitude spectra of the pressure and in the amplitude spectra of the velocity components fluctuations measured under the hydraulic jump.

Moreover, the SPH numerical model of the flow allows one to extend the statistical analysis of the experiments, analysing the oscillating phenomena also through the computation of spectra of the surface profile elevations, velocity components and pressure fluctuations, of flow fields of the variables of interest and of pointwise correlation coefficients of velocity and pressure fluctuations. These new data lead to a more detailed characterization of the oscillating characteristics of this type of hydraulic jumps, which originate from the alternation between different hydraulic jump types, and lead, downstream of the hydraulic jump, to the propagation of surface waves and of high-speed regions alternatively located along the bottom or below the free surface.

References

1. Abdel Ghafar A, Mossa M, Petrillo A (1995) Scour from flowdownstream of a sluice gate after a horizontal apron. In: Varma CVJ, Rao ARG (eds) 6th International symposium on river sedimentation—management of sediment—philosophy, aims, and techniques, New Delhi, Oxford & IBH Publishing Co. Pvt. Ltd., pp 1069–1088

2. Altomare C, Suzuki T, Domínguez JM, Crespo AJC, Gómez-Gesteira M, Caceres I (2015) A hybrid numerical model for coastal engineering problems. In: Proceedings of 34th international conference on coastal engineering (ICCE), http://dx.doi.org/10.9753/icce.v34.waves.60

3. Antuono M, Colagrossi A, Marrone S, Molteni D (2010) Free-surface flows solved by means of SPH schemes with numerical diffusive terms. Comp Phys Commun 181(3):532–549

4. Antuono M, Colagrossi A, Marrone S (2012) Numerical diffusive terms in weakly-compressible SPH schemes. Comp Phys Commun 183(12):2570–2580

5. Ataie-Ashtiani B, Shobeyri G (2008) Numerical simulation of landslide impulsive waves by incompressible smoothed particle hydrodynamics. Int J Numer Meth Fluids 56:209–232

6. Bayon A, Valero D, García-Bartual R, Jos F, Valles-MorF J, Lopez-Jim P (2016) Performance assessment of OpenFOAM and FLOW-3D in the numerical modeling of a low Reynolds number hydraulic jump. Environ Model Softw 80:322–335

7. Ben Meftah M, Mossa M (2006) Scour holes downstream of bed sills in low-gradient channels. J Hydraul Res 44(4):497–509

8. Ben Meftah M, De Serio F, Mossa M, Pollio A (2007) Analysis of the velocity field in a large rectangular channel with lateral shockwave. Environ Fluid Mech 7:519–536. https://doi.org/10.1007/s10652-007-9034-7

9. Ben Meftah M, De Serio F, Mossa M, Pollio A (2008) Experimental study of recirculating flows generated by lateral shock waves in very large channels. Environ Fluid Mech 8:215–238. https://doi.org/10.1007/s10652-008-9057-8

10. Ben Meftah M, Mossa M, Pollio A (2010) Considerations on shock wave/boundary layer interaction in undular hydraulic jumps in horizontal channels with a very high aspect ratio. Eur J Mech B Fluids 29:415–429. https://doi.org/10.1016/j.euromechflu.2010.07.002

11. Capone T, Panizzo A, Monaghan JJ (2010) SPH modelling of water waves generated by submarine landslides. J Hydraul Res 48:80–84

12. Cartwright BK, Chhor A, Groenenboom P (2010) Numerical simulation of a helicopter ditching with emergency flotation devices. In: Proceedings of 10th SPHERIC international workshop, pp 98–105

13. Carvalho R, Lemos C, Ramos C (2008) Numerical computation of the flow in hydraulic jump stilling basins. J Hydraul Res 46(6):739–752

14. Chanson H, Brattberg T (2000) Experimental study of the air-water shear flow in a hydraulic jump. Int J Multiph Flow 26(4):583–607

15. Chanson H, Carvalho R (2015) Hydraulic jumps and stilling basins. Chapter 4. In: Chanson H (ed) Energy dissipation in hydraulic structures. CRC Press, Taylor & Francis Group, A. Balkema Book

16. Chanson H, Gualtieri C (2008) Similitude and scale effects of air entrainment in hydraulic jumps. J Hydraul Res 46(1):35–44

17. Chippada S, Ramaswamy B, Wheeler MF (1994) Numerical simulation of hydraulic jump. Int J Numer Meth Eng 37(8):1381–1397

18. Chow VT (1959) Open channel hydraulics. McGraw-Hill, New York

19. Dalrymple RA, Rogers BD (2006) Numerical modelling of waves with the SPH method. Coast Eng 53:131–147

20. De Padova D, Dalrymple RA, Mossa M, Petrillo AF (2008) An analysis of SPH smoothing function modelling a regular breaking wave. In: Proceedings of national conference on XXXI Convegno Nazionale di Idraulica e Costruzioni Idrauliche, Perugia, Italy, p 182

21. De Padova D, Mossa M, Sibilla S (2009) Laboratory experiments and SPH modelling of hydraulic jumps. In: Le Touzé D (ed) Proceedings of the international conference on 4th Spheric Workshop, Nantes, 4th Spheric Workshop LOC, Nantes, pp 255–257

22. De Padova D, Mossa M, Sibilla S, Torti E (2013) 3D SPH modelling of hydraulic jump in a very large channel. J Hydraul Res 51:158–173

23. De Padova D, Dalrymple RA, Mossa M (2014) Analysis of the artificial viscosity in the smoothed particle hydrodynamics modelling of regular waves. J Hydraul Res 52:836–848

24. De Padova D, Mossa M, Sibilla S (2016) SPH numerical investigation of the velocity field and vorticity generation within a hydrofoil-induced spilling breaker. Environ Fluid Mech 16(1):267–287

25. De Padova D, Mossa M, Sibilla S (2017) SPH modelling of hydraulic jump oscillations at an abrupt drop. Water 90:790–814

26. Dehnen W, Aly H (2012) Improving convergence in smoothed particle hydrodynamics simulations without pairing instability. Mon Not R Astron Soc 425:1068–1082
27. Domínguez JM, Crespo AJC, Gómez-Gesteira M, Marongiu JC (2010) Neighbour lists in smoothed particle hydrodynamics. Int J Numer Meth Fluids 67(12):2026–2042
28. Escue A, Cui J (2010) Comparison of turbulence models in simulating swirling pipe flows. Appl Math Model 34:2840–2849
29. Espa P, Sibilla S, Gallati M (2008) SPH simulations of a vertical 2-D liquid jet introduced from the bottom of a free-surface rectangular tank. Adv Appl Fluid Mech 3:105–140
30. Federico I, Marrone S, Colagrossi A, Aristodemo F, Antuono M (2012) Simulating 2D open-channel flows through an SPH model. Eur J Mech B Fluids 34:35–46
31. Fourtakas G, Rogers BD, Laurence DR (2014) Modelling sediment resuspension in industrial tanks using SPH. La Houille Blanche 2014(2):39–45
32. Gingold RA, Monaghan JJ (1977) Smoothed particle hydrodynamics: theory and application to non-spherical stars. Monthly Not Royal Astron Soc 181:375–389
33. Gomez-Gesteira M, Rogers BD, Dalrymple RA, Crespo AJC (2010) State-of-the-art of classical SPH for free-surface flows. J Hydraul Res 48:6–27
34. Grenier N, Le Touzé D, Colagrossi A, Antuono M, Colicchio G (2013) Viscous bubbly flow simulation with an interface SPH model. Ocean Eng 69:88–102
35. Gualtieri C, Chanson H (2007) Experimental analysis of Froude number effect on air entrainment in the hydraulic jump. Springer Environ Fluid Mech 7(3):217–238
36. Gualtieri C, Chanson H (2010) Effect of Froude number on bubble clustering in a hydraulic jump. J Hydraul Res 48(4):504–508
37. Guo B, Langrish TAG, Fletcher DF (2001) An assessment of turbulence models applied to the simulation of a two-dimensional submerged jet. Appl Math Model 25:635–653
38. Hager WH, Bretz NV (1986) Hydraulic jumps at positive and negative steps. J Hydraul Res 24(4):237–252
39. Hu XY, Adams NA (2009) A constant-density approach for incompressible multi-phase SPH. J Comput Phys 228(6):2082–2091
40. Jonsson P, Andreasson P, Gunnar J, Hellström I, Jonsén P, Lundström TS (2016) Smoothed Particle Hydrodynamic simulation of hydraulic jump using periodic open boundaries. Appl Math Model 40(19–20):8391–8405
41. Launder BE, Spalding DB (1974) The numerical computation of turbulent flows. Comp Meth Appl Mech Eng 3:269–289
42. Lind SJ, Stansby PK, Rogers BD, Lloyd PM (2015) Numerical predictions of water-air wave slam using incompressible-compressible smoothed particle hydrodynamics. Appl Ocean Res 49:57–71
43. Liu GR, Liu MB (2007) Smoothed particle hydrodynamics—a meshfree particle methods. World Scientific Publishing, Singapore
44. Liu GR, Liu MB (2010) Smoothed particle hydrodynamics (SPH): an overview and recent developments. Arch Comput Methods Eng 17:25–76
45. Long D, Rajaratnam N, Steffler PM, Smy PR (1991) Structure of flow in hydraulic jumps. J. Hydraul Res 29(2):207–218
46. Lucy L (1977) A numerical approach to the testing of fusion process. J Astron 82:1013–1024
47. Ma F, Hou Y, Prinos P (2001) Numerical calculation of submerged hydraulic jumps. J Hydraul Res 39(5):493–503
48. Manenti S, Sibilla S, Gallati M, Agate G, Guandalini R (2012) SPH Simulation of sediment flushing induced by a rapid water flow. J Hydraul Eng 138(3):272–284
49. Manenti S, Pierobon E, Gallati G, Sibilla S, D'Alpaos L, Macchi EG, Todeschini S (2016) Vajont disaster: smoothed particle hydrodynamics modeling of the post-event 2D experiments. J Hydraul Eng 142(05015007):1–11
50. Marrone S, Bouscasse B, Colagrossi A, Antuono M (2012) Study of ship wave breaking patterns using 3D parallel SPH simulations. Comput Fluids 69:54–66
51. Meireles IC, Bombardelli FA, Matos J (2014) Air entrainment onset in skimming flows on steep stepped spillways: an analysis. J Hydraul Res 52(3):375–385
52. Monaghan JJ (1992) Simulating free surface flows with SPH. J Comput Phys 110(2):399–406
53. Monaghan JJ (2005) Smoothed particle hydrodynamics. Rep Prog Phys 68:1703–1759
54. Mohaghan JJ, Kocharyan A (1995) SPH simulation of multi-phase flow. Comput Phys Commun 87:225–235
55. Mokos A, Rogers BD, Stansby PK (2015) Multiphase SPH modelling of violent hydrodynamics on GPUs. Comput Phys Commun 196:304–316
56. Moore WL, Morgan CW (1959) Hydraulic jump at an abrupt drop. Trans ASCE 124:507–524

57. Mossa M, Tolve U (1998) Flow visualization in bubbly two-phase hydraulic jump. J Fluids Eng ASME 120(1):160–165
58. Mossa M (1999) On the oscillating characteristics of hydraulic jumps. J Hydraul Res 37(4):541–558
59. Mossa M, Petrillo A, Chanson H (2003) Tailwater level effects on flow conditions at an abrupt drop. J Hydraul Res 41(1):39–51
60. Mossa M, Petrillo A, Chanson H (2004) Discussion on "Tailwater level effects on flow conditions at an abrupt drop". J Hydraul Res 43(2):217–224
61. Mossa M (2005) Discussion on "Relation of surface roller eddy formation and surface fluctuation in hydraulic jumps by K.M. Mok". J Hydraul Res 43(5):588–592
62. Mossa M (2008) Experimental study of the flow field with spilling type breaking. J Hydraul Res 46:81–86
63. Murzyn F, Mouaze D, Chaplin J (2005) Optical fiber probe measurements of bubbly flow in hydraulic jumps. Elsevier Int J Multiph Flow 31(1):141–154
64. Nazari F, Jin Y-C, Shakibaeinia A (2012) Numerical analysis of jet and submerged hydraulic jump using moving particle semi-implicit method. Can J Civ Eng 39:495–505
65. Nebbia G (1940a) Sui dissipatori a salto di Bidone –Basi teoriche, L'Energia Elettrica, fasc. III—vol XVII, pp 125–138
66. Nebbia G (1940b) Sui dissipatori a salto di Bidone –Ricerca sperimentale, L'Energia Elettrica, fasc. VI—vol XVII, pp 327–355
67. Nebbia G (1941) Sui dissipatori a salto di Bidone –Norme di proporzionamento, L'Energia Elettrica, fasc. VII—vol XVIII, pp 441–454, 533–546
68. Nebbia G (1942) Su taluni fenomeni alternativi in correnti libere, L'Energia Elettrica, fasc. I—vol XIX, pp 1–10
69. Ni X, Feng WB, Wu D (2014) Numerical simulations of wave interactions with vertical wave barriers using the SPH method. Int J Numer Meth Fluids 76(4):223–245
70. Ohtsu I, Yasuda Y (1991) Transition from supercritical to subcritical flow at an abrupt drop. J Hydraul Res 29(3):309–328
71. Pugliese Carratelli E, Viccione G, Bovolin V (2016) Free surface flow impact on a vertical wall: a numerical assessment. Theor Comput Fluid Dyn 30(5):403–414
72. Rajaratnam N, Subramanya K (1967) Flow equation for the sluice gate. J Irrig Drain Eng 93(1):167–186
73. Randles PW, Libersky LD (1996) Smoothed particle hydrodynamics: some recent improvements and applications. Comput Methods Appl Mech Eng 139(1–4):375–408
74. Resch F, Leutheusser H (1972) Reynolds stress measurements in hydraulic jumps. J Hydraul Res 10(4):409–430
75. Shao S (2006) Incompressible SPH simulation of wave breaking and overtopping with turbulence modeling. Int J Numer Meth Fluids 50:597–621
76. Sibilla S (2008) A SPH-based method to simulate local scouring. In: Proceedings of 19th IASTED international conference on modelling and simulation MS 2008, Ville de Quebec, pp 9–14
77. Sibilla S (2015) An algorithm to improve consistency in smoothed particle hydrodynamics. Comput Fluids 118:148–158
78. Ulrich C, Leonardi M, Rung T (2013) Multi-physics SPH simulation of complex marine-engineering hydrodynamic problems. Ocean Eng 64:109–121
79. Viccione G, Bovolin V, Carratelli EP (2008) 2008 Defining and optimizing algorithms for neighbouring particle identification in SPH fluid simulations. Int J Numer Meth Fluids 58(6):625–638
80. Viccione G, Bovolin V (2011) Simulating triggering and evolution of debris-flows with SPH. In: International conference on debris-flow hazards mitigation: mechanics, prediction, and assessment, proceedings, pp 523–532
81. Violeau D (2004) One and two-equations turbulent closures for smoothed particle hydrodynamics. In: Proceedings of 6th international conference hydroinformatics, pp 87–94
82. Violeau D (2012) Fluid mechanics and the SPH method: theory and applications. Oxford University Press, Oxford
83. Violeau D, Piccon S, Chabard J-P (2002) Two attempts of turbulence modelling in smoothed particle hydrodynamics. Advances in fluid modelling and turbulence measurements. World Scientific, Singapore, pp 339–346
84. Violeau D, Rogers BD (2016) Smoothed particle hydrodynamics (SPH) for free-surface flows: past, present and future. J Hydraul Res 54(1):1–26
85. Wang H, Murzyn F, Chanson H (2014) Total pressure fluctuations and two-phase flow turbulence in hydraulic jumps. Exp Fluids 55:1847
86. Wang H, Chanson H (2015) Experimental study of turbulent fluctuations in hydraulic jumps. J Hydraul Eng 141(7):04015010

87. Wang ZB, Chen R, Wang H, Liao Q, Zhu X, Li SZ (2016) An overview of smoothed particle hydrodynamics for simulating multiphase flow. Appl Math Model 40:9625–9655
88. Wendland H (1995) Piecewise polynomial, positive definite and compactly supported radial functions of minimal degree. Adv Comput Math 4:389–396
89. Yakhot V, Orszag S, Thangam S, Gatski T, Speziale C (1992) Development of turbulence models for shear flows by a double expansion technique. Phys Fluids A 4(7):1510–1520
90. Zhang A, Cao X-Y, Ming F, Zhang Z-F (2013) Investigation on a damaged ship model sinking into water based on three dimensional SPH method. Appl Ocean Res 42:24–31
91. Zhang W, Liu M, Zhu DZ, Rajaratnam N (2014) Mean and turbulent bubble velocities in free hydraulic jumps for small to intermediate Froude numbers. J Hydraul Eng 140(11):04014055